The Astrophysical Journal, 958:185 (13pp), 2023 December 1 https://doi.org/10.3847/1538-4357/ad02f3

A Comprehensive Observational Study of the FRB 121102 Persistent Radio Source

Ge Chen, Vikram Ravi, and Gregg W. Hallinan
Cahill Center for Astronomy and Astrophysics, MC 249-17, California Institute of Technology, Pasadena, CA 91125, USA; gcchen@caltech.edu

Received 2022 January 7; revised 2023 October 4; accepted 2023 October 11; published 2023 November 27

Abstract

FRB 121102 is the first fast radio burst to be spatially associated with a persistent radio source (QRS 121102), the nature of which remains unknown. We constrain the physical size of QRS 121102 by measuring its flux-density variability with the VLA from 12 to 26 GHz. Any such variability would likely be due to Galactic refractive scintillation and would require the source radius to be $\lesssim 10^{17}$ cm at the host-galaxy redshift. We found the radio variability to be lower than the scintillation theory predictions for such a small source, leaving open the possibility for non-AGN models for QRS 121102. In addition, we roughly estimated the mass of any potential supermassive black hole (BH) associated with QRS 121102 from the line width of the host-galaxy Hα emission using a new optical spectrum from the Keck Observatory. The line width indicates a supermassive BH mass of $\lesssim 10^{4\sim5} M_{\odot}$, too low for the observed radio luminosity and X-ray luminosity constraints, if QRS 121102 were an AGN. Finally, some dwarf galaxies that host supermassive BHs may be the stripped cores of massive galaxies during tidal interactions with companion systems. We find no nearby galaxy at the same redshift as the QRS 121102 host from low-resolution Keck spectra or the PanSTARRS catalog. In conclusion, we find no evidence supporting the hypothesis that QRS 121102 is an AGN. We instead argue that the inferred size and flat radio spectrum favor a plerion interpretation. We urge continued broadband radio monitoring of QRS 121102 to search for long-term evolution.

Unified Astronomy Thesaurus concepts: Radio transient sources (2008); High energy astrophysics (739); Radio bursts (1339); Extragalactic radio sources (508)

1. Introduction

Fast radio bursts (FRBs) are a class of transient phenomena wherein energies $\gtrsim 10^{35}$ erg are released on timescales of $\ll 1$ s at radio wavelengths (e.g., Lorimer et al. 2007). The progenitor and emission processes of FRBs remain uncertain. Hundreds of FRB sources have been reported, and more than 20 of them have been found to repeat (e.g., CHIME/FRB Collaboration et al. 2021). Repeaters and nonrepeaters are reported to show statistically different characters (luminosity, pulse width, temporal–spectral structures, etc.), yet it remains unclear whether or not they originate from two distinct populations. FRB 121102 (hereafter QRS 121102) was the first repeater detected (Scholz et al. 2016; Spitler et al. 2016) and so far one of the most extensively studied FRB sources. The bursts are found to have an ~160 day periodicity (Cruces et al. 2021), and the source has been localized within a star-forming region of a low-metallicity dwarf galaxy at a redshift of 0.19273 (Bassa et al. 2017; Marcote et al. 2017; Tendulkar et al. 2017), giving a luminosity distance of 971 Mpc (using the recent Planck results implemented in *astropy*: $H_0 = 67.4\ \mathrm{km\ s^{-1}\ kpc^{-1}}$, $\Omega_m = 0.315$, $\Omega_\Lambda = 0.685$; Planck Collaboration et al. 2020).

QRS 121102 is one of only two FRBs reported to be spatially associated with persistent radio emission of unknown origin (Tendulkar et al. 2017; Niu et al. 2022). In the case of QRS 121102, the centroid of the persistent emission is within 12 mas (40 pc; 95% confidence level) from the FRB source. The emission shows a flat spectrum from ~400 MHz to ~6 GHz (flux density ≈200 μJy) and decreases at higher frequencies (166 ± 9, 103 ± 7, and 66 ± 7 μJy at 10, 15, and 22 GHz, respectively; Chatterjee et al. 2017; Resmi et al. 2021). It remains unresolved by very long baseline interferometry (VLBI) at 5 GHz, indicating a radius below ~0.2 mas, or $\sim 10^{18}$ cm (0.35 pc) at the host galaxy redshift (Tendulkar et al. 2017). A flux density amplitude modulation of ~30% has been reported at 3 GHz (Chatterjee et al. 2017), consistent with refractive scintillation by the Milky Way interstellar medium (ISM; e.g., Romani et al. 1986; Walker 1998). No X-ray counterpart has been detected with XMM-Newton and Chandra (Chatterjee et al. 2017).

If we remain agnostic regarding models for the origin of FRBs, a compact radio source like that associated with QRS 121102, with a luminosity of $\sim 2 \times 10^{29}\ \mathrm{erg\ s^{-1}\ Hz^{-1}}$, would most likely be ascribed to active galactic nucleus (AGN) activity. Several AGN-like radio sources of similar luminosities have been reported to be hosted by dwarf galaxies (e.g., Mezcua et al. 2019; Reines et al. 2020). Although Tendulkar et al. (2017) found the host galaxy optical spectrum to be consistent with intense star formation based on the Baldwin, Phillips, and Terlevich (BPT) diagnostics (Baldwin et al. 1981), it is rare but not unheard of (at the ~0.1% level; Sabater et al. 2019) for galaxies classified as star-forming according to BPT diagnostics to host radio-loud AGN. This may be substantially more common among the dwarf galaxy population; the majority of the Reines et al. (2020) sample of dwarf galaxies with optical spectra hosting candidate radio AGN are classified as star-forming on BPT diagrams. The radio source associated with QRS 121102 is too compact and luminous to be associated with star formation activity (Chatterjee et al. 2017). Other possible origins include a supernova afterglow powered by interaction with a dense circumstellar medium (Dong et al. 2021), the afterglow of a long-duration gamma-ray burst (LGRB; e.g., Berger et al. 2003), and an extreme pulsar wind nebula (PWN; e.g., Margalit & Metzger 2018).

Table 1
VLA Observations and Results

Obs.	Epoch (YYYY-MM-DD hh:mm)	Band	3C 147 (f0) (Jy)	J0555+3948 (f1) (mJy)	J0518+3306 (f2) (mJy)	QRS 121102 (f3) (μJy)
1	2017-05-29 16:09	*K*	1.994 ± 0.010	1956.5 ± 2.5	153.1 ± 5.3	56.6 ± 8.2
2	2017-06-03 16:43	*K*	2.010 ± 0.013	2135.8 ± 3.4	143.9 ± 2.5	52.4 ± 7.0
3	2017-06-08 08:19	*U*	2.82 ± 0.11	2242 ± 15	200.2 ± 1.7	67 ± 13
4	2017-06-10 21:25	*U*	2.857 ± 0.010	2565 ± 30	214.5 ± 5.7	118.0 ± 5.5
5	2017-06-11 16:32	*U*	2.799 ± 0.018	2431.2 ± 6.4	158.2 ± 2.5	82.1 ± 6.4
6	2017-08-10 12:31	*K*	2.050 ± 0.026	2148.4 ± 7.5	193.6 ± 5.4	109 ± 14
	2017-08-10 06:04	*U*	2.804 ± 0.026	2217.7 ± 6.0	144.0 ± 4.3	63.5 ± 6.3

Table 2
VLA Targets

Field	Target	R.A.	Decl.	Intention	Single Scan Duration (minute)
0	J0542+4951 (3C 147)	$05^{h}42^{m}36\overset{s}{.}1$	$+49°51'07\overset{''}{.}2$	Flux and bandpass calibrator	6
1	J0555+3948	$05^{h}55^{m}30\overset{s}{.}8$	$+39°48'49\overset{''}{.}2$	Phase calibrator 1[a]	1.5
2	J0518+3306	$05^{h}18^{m}05\overset{s}{.}1$	$+33°06'13\overset{''}{.}4$	Phase calibrator 2[b]	1.5
3	QRS 121102	$05^{h}31^{m}58\overset{s}{.}7$	$+33°08'52\overset{''}{.}5$	Science	10

Notes.
[a] Used as the phase calibrator during our CASA imaging process.
[b] Treated as a science target during our CASA imaging process.

Table 3
Summary of Optical Observations

Date (YYYY-MM-DD)	Instrument	Grating, Grism (Red, Blue)	λ (Red, Blue) (Å)	Slit (arcmin)	Resolution (1σ) (Å)	Exposure (minute)
2018-10-12	LRIS	1200/7500, 400/3400	NA	Long 1.0	∼1	80[a]
2017-01-26	LRIS	400/8500, 600/4000	5462 ∼10318, 3122 ∼5603	Long 1.5	∼4	50

Note.
[a] Each exposure is 20 minutes. The total exposure time is 80 minutes when combining all four exposures and 40 minutes after excluding the two exposures polluted by cosmic rays (see Section 3.2).

In this paper, we investigate the nature of the persistent radio source associated with QRS 121102 using new data from the Karl G. Jansky Very Large Array (VLA) and the Low Resolution Imaging Spectrometer (LRIS) at the Keck Observatory. We adopt the host redshift of 0.19273 (Tendulkar et al. 2017) for all relevant calculations hereafter. In Section 2, we describe the observations. In Section 3, we first measure the flux density modulation of QRS 121102 in the *K* (18–26 GHz) and *Ku* (12–18 GHz) bands, where refractive scintillation is expected to produce larger modulations than previously observed at 5 GHz. We also separately investigate the hypothesis that QRS 121102 is powered by a supermassive or intermediate-mass black hole (BH) using a medium-resolution LRIS spectrum and evaluate whether or not the host galaxy belongs to a galaxy group using the low-resolution LRIS spectra. In Section 4, we first constrain the size of QRS 121102 by comparing its flux density modulation with that predicted by scattering theory. In addition, we compare the AGN population with our dynamical BH mass estimation, stellar mass estimation, and radio and X-ray luminosity constraints. We conclude in Section 5 that an AGN hypothesis for QRS 121102 is unlikely.

2. Observations

2.1. VLA Radio Observations

We have observed the persistent radio source (QRS 121102) in the VLA *K* (18–26 GHz) and *Ku* (12–18 GHz) bands using the C configuration. The channel width was 2 MHz, and the integration time was 3 s for the *K*-band observations and 2 s for the *Ku*-band observations. The observations include six epochs from 2017 May 29 to 2017 August 10 (Table 1). In each epoch, the observation started with a single scan of the primary calibrator, 3C 147 (field 0), for flux scale and bandpass calibration and then a few cycles of phase calibrator 1, J0555+3948 (field 1); phase calibrator 2, J0518+3306 (field 2); and QRS 121102 (field 3; Table 2).

2.2. Keck Optical Observations

The optical spectra used in this work were obtained using Keck/LRIS (Table 3). We obtained two types of observations. One, with medium spectral resolution, was used to measure the spectral width of the Hα emission line associated with the QRS 121102 host galaxy. The other, with low spectral resolution, used two slit orientations to obtain spectra of galaxies immediately adjacent to the QRS 121102 host.

The medium-resolution spectrum of the QRS 121102 host was obtained on 2018 October 12 using the $1\farcs0$ long slit and the D560 dichroic. The red side used the grating with 1200 lines mm^{-1} blazed at 7500 Å and targeted the Hα emission.

Low-resolution spectra of the host and nearby sources were obtained on 2017 January 26 using the $1\farcs5$ long slit and the 560 dichroic. The grating used on the red side has 400 lines mm^{-1} blazed at 8500 Å, covering wavelengths from about 5462 to 10318 Å, with a dispersion of 1.86 Å pixel^{-1}. We estimate the spectral resolution to be ~ 4 Å (1σ) from the weighted average width of the four isolated sky lines (5577.0, 5898.0, 6315.7, and 7257.4 Å). On the blue side, the grism has 600 lines mm^{-1} blazed at 4000 Å, covering wavelengths from 3122 to 5603 Å. Standard stars were observed for the flux response calibration, arc lamp spectra were obtained for the wavelength calibration, and bias frames were taken for the bias subtraction. The flat field was generated using dome flats.

3. Data Analysis and Results

3.1. VLA Flux Density Measurements

In this section, we describe how we measure the radio flux density of QRS 121102 in each epoch.

The visibility data were calibrated and imaged using Common Astronomy Software Applications (CASA) following the standard procedures (task names shown in parentheses).[1] In the calibration, the VLA antenna positions were updated (*gencal*). The primary calibrator, 3C 147, was used to find the absolute scale of the gain amplitudes by referring to the standard flux density (*setjy*) and to correct for the instrumental delay and the complex antenna-response variation with frequency (*bandpass*). The complex gain solutions (both amplitude and phase) were obtained from phase calibrator 1, J0555+3948, which is $\sim 8°$ away from QRS 121102 (CASA task *gaincal*), and the gain amplitudes were properly scaled using the absolute scale obtained using just 3C 147 (*fluxscale*). All calibration solutions were then applied (*applycal*) to QRS 121102, as well as the fainter phase calibrator 2, J0518+3306 ($\sim 2°$ away from QRS 121102). After calibration, potential radio frequency interference (RFI) and internally generated signals were removed by flagging out narrowband spikes in the spectra (*flagdata*). In epoch 3, one scan of QRS 121102 was removed, as it was several times brighter than the others (within 30 minutes apart) due to strong RFI, or perhaps a passing cloud. The calibrated visibility data were binned to 20 s and 500 kHz to speed up synthesis imaging using the CASA task (*split*). The data were gridded and Fourier transformed, and the synthesized beam was deconvolved (*tclean*). The FWHM of the synthesized beam was $\sim 1\farcs5$ (major axis) × $1\farcs2$ (minor axis) in the *Ku* band and $\sim 1\farcs3$ (major axis) × $0\farcs9$ (minor axis) in the *K* band in the C configuration. Our images were created using a small cell size of $0\farcs1 \times 0\farcs1$ and a Briggs robust weighting of 0.5 (Briggs 1995).

We measured the flux density of each source from the images by fitting each with a 2D Gaussian model (*imfit*; Figure 1). We obtained the flux density of those point sources (based on the criterion implemented by the CASA *imfit* task) from the peak and the others from the integrated flux density within each fitting region. Uncertainties were calculated by propagation of errors of the 2D fitting model. Table 1 lists the results, and Figure 2 shows the flux density light curves in both bands.

The angular size of QRS 121102 has been reported to be under ~ 0.2 mas at 5 GHz as measured by VLBI (Marcote et al. 2017). It is expected to be unresolved in our observations, where the beam FWHM is $\sim 1\farcs4$ in the *Ku* band and $\sim 0\farcs9$ in the *K* band. In our images, the 2D Gaussian fitting results show that QRS 121102 is a point source in all but epoch 3, where the image is marginally resolved as $1\farcs13 \pm 0\farcs61$ along the major axis and $0\farcs49 \pm 0\farcs22$ along the minor axis (FWHM, deconvolved from the beam). This is likely due to the remaining phase errors in the calibration solution, as the image of phase calibrator 2, J0518+3306, appears highly distorted. The errors were removed by phase-only self-calibration in field 2 but not in field 3 for the reasons outlined below.

In field 3, our observations of QRS 121102 were affected by a bright source, NVSS J053153+331014, that is $\approx 1\farcm8$ (twice the primary beam FWHM in the *Ku* band) away from the pointing center (QRS 121102) and over 1 order of magnitude brighter (≈ 3 mJy in flux density before correcting for primary beam attenuation). To reduce the associated errors, we performed self-calibration (phase only) for NVSS J053153+331014 and QRS 121102 simultaneously. We also tried to remove the flux density contribution from NVSS J053153+331014 modeled from self-calibration and then subtract the model visibility from the corrected visibility data. Neither attempt made a significant improvement on the image of QRS 121102, since self-calibration failed to correct the beam model error far away from the pointing center.

In addition, there might be remaining calibration errors, since the flux densities of the two phase calibrators, J0555+3948 and J0518+3306, also vary by $\sim 4\%$ and $\sim 10\%$ throughout the epochs in each band (Figure 2). The variations are likely not intrinsic to the source for two reasons. (1) J0555+3948 has been reported to vary by 2.0% on a timescale of 251 days at 33 GHz and 3.4% on a timescale of 293 days at 16 GHz (Franzen et al. 2009). It is unlikely to show a greater variability on a timescale of days, as has been observed in this work (e.g., epochs 3, 4, and 5). (2) More importantly, the flux density light curve of QRS 121102 shows a moderate positive correlation with that of J0555+3948 and a strong positive correlation with that of J0518+3306, with correlation coefficients of 0.67 and 0.91, respectively. To reduce potential calibration errors, in each epoch, we rescaled the flux density measurements of QRS 121102 by those of the two phase calibrators (Figure 3). We adopt the flux density scaled by J0518+3306 (phase calibrator 2) thereafter, since it has a smaller angular separation from QRS 121102.

3.2. Keck/LRIS Medium-resolution Spectral Analysis

The LRIS data were processed using the LRIS automated reduction pipeline (LPipe; Perley 2019) following standard procedures: subtract the bias, make flat fields and apply flat-field correction, remove cosmic-ray pixels, model and remove sky lines, perform wavelength calibration by referring to the arc lamp spectra, and determine the flux response function by observing standard reference stars. The processed 2D spectrum targets the Hα emission.

The width of the Hα emission line is produced by multiple effects (Rybicki & Lightman 1979):

---

[1] CASA is a software package developed by the NRAO.

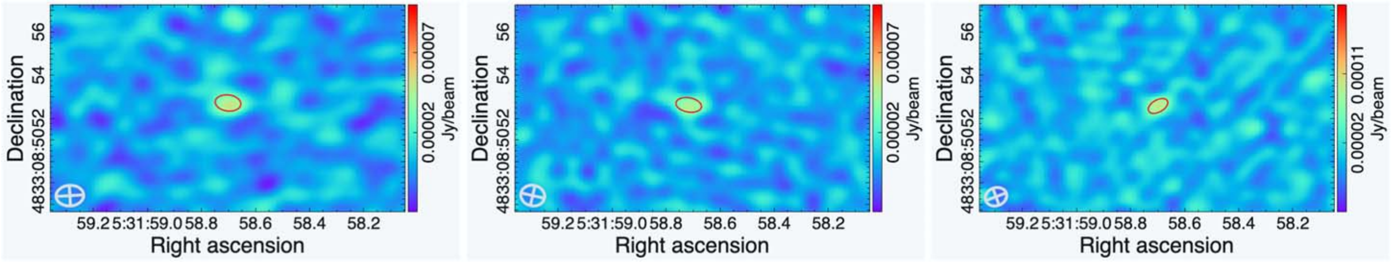

Epoch 1 (K) Epoch 2 (K) Epoch 6 (K)

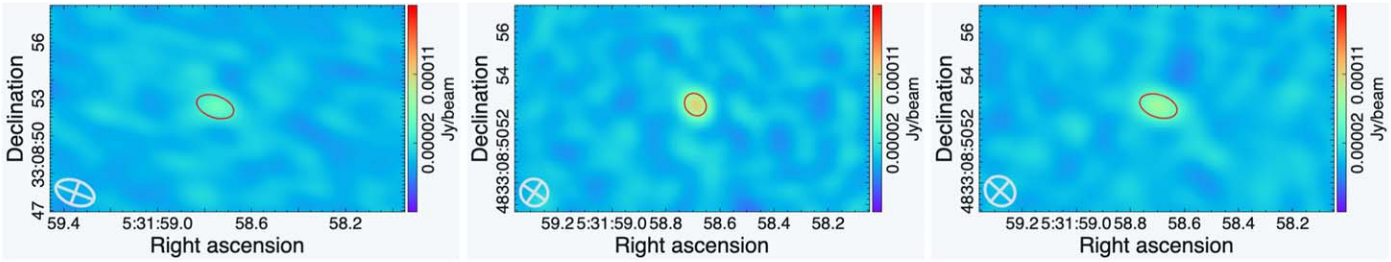

Epoch 3 (U) Epoch 4 (U) Epoch 5 (U)

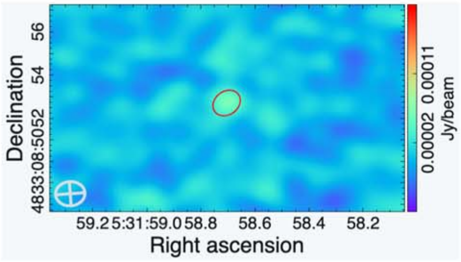

Epoch 6 (U)

Figure 1. VLA images (in J2000 coordinates) of QRS 121102 in seven epochs, with the band indicated in parentheses. The color scale represents the flux density in janskys per beam (see color bar). The light gray circle (bottom left corner of each image) shows the synthesized beam size (1σ), and the red circle shows the 1σ 2D Gaussian fitting results convolved with the synthesized beam. The position angles of the best-fit results are consistent with those of the clean beams within 1σ in all cases where the source is unresolvable.

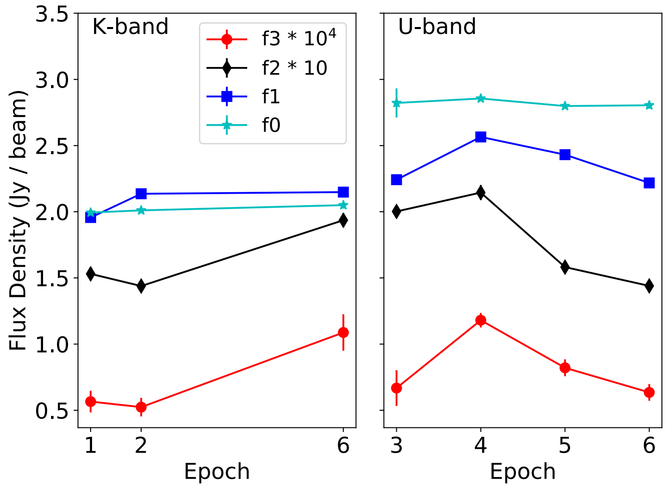

Figure 2. Flux density light curve of the *K* (left) and *Ku* (right) bands. f3, f2, f1, and f0 represent the flux density of QRS 121102 (red circles), phase calibrator 2 (black diamonds), phase calibrator 1 (blue squares), and the prime calibrator (cyan stars), respectively. f3 and f2 are scaled by 10^4 and 10 times for display. Details of the observations are shown in Tables 1 and 2.

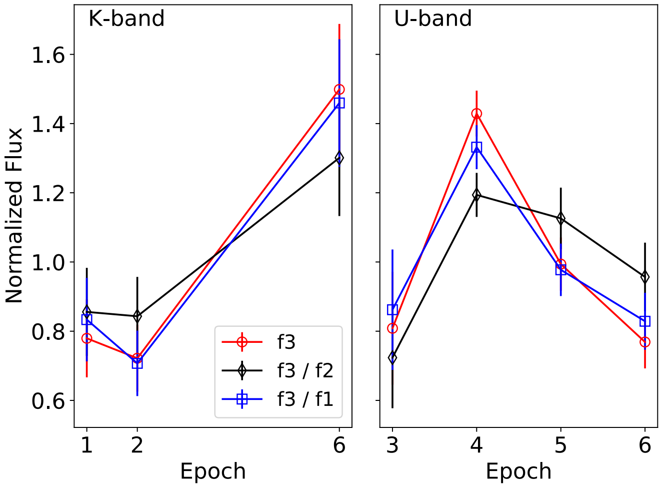

Figure 3. Normalized (and scaled) flux density light curve of the *K* (left) and *Ku* (right) bands. f3, f2, and f1 represent the flux density of QRS 121102, phase calibrator 2, and phase calibrator 1, respectively. Red open circles (f3) show the normalized flux density of QRS 121102, black open diamonds (f3/f2) show the flux density of QRS 121102 divided by those of phase calibrator 2 and then normalized to average at unity, and blue open squares (f3/f1) are the flux density of QRS 121102 divided by those of phase calibrator 1 and then normalized to average at unity.

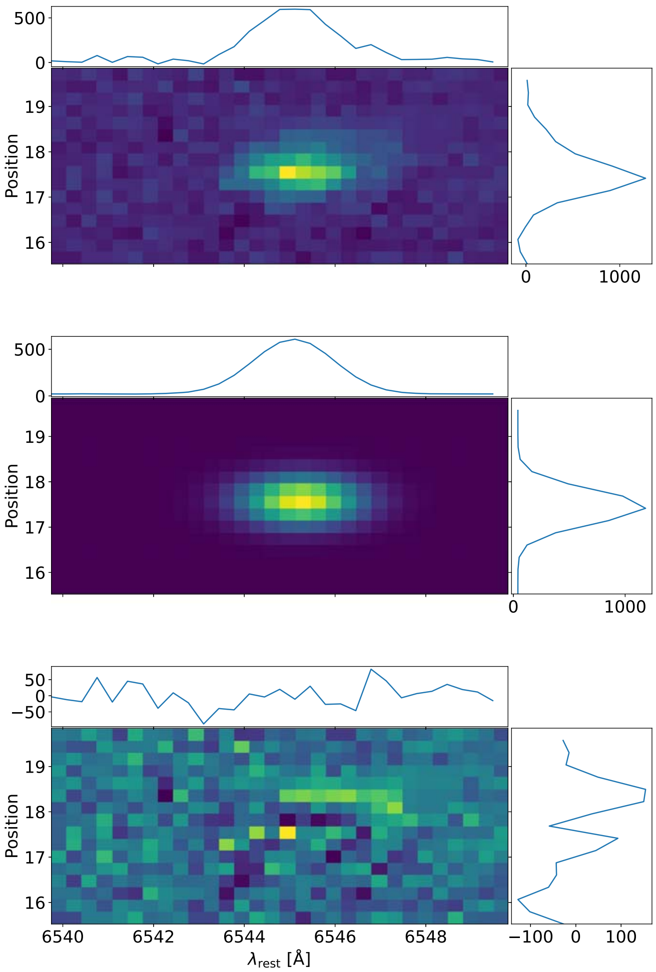

Figure 4. 2D medium-resolution LRIS spectrum of the host galaxy of QRS 121102. Wavelength has been converted to the rest frame using the previously reported redshift of $z = 0.19273$ (Tendulkar et al. 2017). Top to bottom, the panels are the observed 2D spectrum, the 2D fitting model, and the residual (data−model). On the top and right of each panel are plots of the data collapsed along the wavelength and position axes, respectively.

1. dynamical velocity dispersion due to gravity,
2. instrumental broadening,
3. random thermal motions,
4. natural broadening, and
5. turbulent motions.

In this section, we test the hypothesis that QRS 121102 is associated with an AGN by using the velocity dispersion to roughly constrain the mass of a potential supermassive BH. The velocity dispersion is estimated from the Hα line width.

The Hα emission line width of the host is determined by fitting the rest-frame 2D spectrum with a 2D Gaussian function whose rotation angle is fixed at zero, plus a constant offset. We convert the observed 2D spectrum of the host into the rest-frame wavelength using a previously reported redshift of 0.19273 (Tendulkar et al. 2017). The width (1σ) of the emission line is 0.9316 ± 0.0026 Å when combining all four exposures and 0.8947 ± 0.0015 Å after removing the two exposures polluted by the nearby cosmic rays (Figure 4). A bright pixel at the center of the Hα emission is seen in the residual (bottom panel of Figure 4), but no extended structure that might impact the emission width result is found.

We then determine the width of the instrumental broadening effects by collapsing the 2D spectrum into 1D and fitting each of the three isolated sky lines in the field with a 1D Gaussian function plus an offset. The instrumental spectral broadening width is given by the weighted mean of the three sky lines' 1σ widths (0.638725 ± 0.000039 Å). The natural broadening width of the Hα line is known to be 0.46 mÅ (e.g., Rybicki & Lightman 1979). The 1σ width of the line is 0.6265 ± 0.0021 Å after quadratically removing the instrumental and natural broadening effects.

The rest-frame line width of a Maxwellian velocity distribution (i.e., Gaussian along the line of sight) is given by Rybicki & Lightman (1979):

$$\frac{\Delta\nu}{\nu_0} = \frac{1}{c}\left(\sigma_v^2 + \frac{2kT}{m_{\rm H}} + v_{\rm turb}^2\right)^{1/2}. \tag{1}$$

Here $\Delta\nu$ Hz is the rest-frame line width (1σ) in frequency, and $\nu_0 = 4.57 \times 10^{14}$ Hz is the frequency of the Hα emission in vacuum. σ_v is the velocity dispersion due to gravity, and $\sqrt{2kT/m_{\rm H}} \approx 12.8$ km s^{-1}is the most probable thermal velocity assuming a gas temperature of 10^4 K (e.g., Draine 2011). $v_{\rm turb}$, the turbulent velocity, is weakly constrained to be $\lesssim 10^3$ km s^{-1} as inferred from the scattering measurements (SMs) of QRS 121102 (Table 2 of Simard & Ravi 2021). We ignore its contribution and find an upper limit of $\sigma_v \lesssim 30$ km s^{-1}.

Assuming that the QRS 121102 host galaxy has a central BH, we estimate its mass using the empirical M–σ relation reported in recent literature. The BH mass is $7.8^{+8.2}_{-5.2} \times 10^4 M_\odot$ using the relation derived from a sample of 88 AGN covering a stellar velocity dispersion σ_* of 30–268 km s^{-1} (Greene & Ho 2006; error bars calculated from the intrinsic scatter found in the relation). A consistent BH mass of $8.8^{16.2}_{-5.8} \times 10^4 M_\odot$ is found using the relation based on 93 low-mass active galaxies (Xiao et al. 2011; σ_* from 31 to 138 km s^{-1}). Other reports show similar results, though an extrapolation of the M–σ relation is required, as the sampled objects cover higher σ_*; the mass is $4.2^{+7.5}_{-2.7} \times 10^4 M_\odot$ (error bars from the intrinsic scatter in the relation) based on a sample of 49 BH mass dynamical measurements in spiral galaxies, S0 galaxies, and elliptical bulges ($\sigma = 67$–385 km s^{-1}; Gültekin et al. 2009) and $\sim 10^4 M_\odot$ from 72 similar objects ($\sigma = 75$–347 km s^{-1}; Ferrarese & Ford 2005; McConnell & Ma 2013). Finally, we note that the measured velocity dispersion is lower than any of those measured from a sample of 35 tidal disruption event host galaxies ($\sigma > 43$ km s^{-1}) reported by Wevers et al. (2017, 2019). This suggests that the BH mass in the QRS 121102 host is lower than the BH masses of the tidal disruption event galaxy sample.

We consider two potential errors in our BH mass estimation. First, the Hα velocity dispersion measurement may not be suitable for the dynamical analysis. The BH mass is usually estimated from the stellar velocity dispersion measured from multiple absorption lines from an optical or IR spectrum. In our observation, these stellar absorption line widths were unavailable due to the limited S/N. Instead, we infer the velocity dispersion from the line width of a single compact Hα emission region (radius <0$''$.24 at 1σ; Kokubo et al. 2017) that is offset from the stellar continuum centroid of the galaxy by $0''.29 \pm 0''.05$ (Tendulkar et al. 2017). The Hα line width reveals the dynamics of the partially ionized warm star-forming gas formed in discrete clouds. If the gas pervades the galaxy, it is expected to have a larger velocity dispersion than the stars due to turbulent motions and provide an upper limit to the BH mass. However, the Hα region is isolated to one part of the host and may not represent the global gas dynamics in the host. This could lead to systematic errors as reported in the dynamical analyses of galaxies with irregular gas and dust distributions (Ho et al. 2002).

However, the dynamical mass implied by the Hα velocity dispersion is comparable to the stellar mass of the QRS 121102 host galaxy inferred using the optical/IR spectral energy distribution. We assume that the system is virialized for an order-of-magnitude estimation. In an ellipsoid, the kinetic energy is dominated by random motions. The virial theorem gives a total stellar mass of $M_* \sim \sigma_v^2 R_{\rm eff}/G \sim 10^8 M_\odot$, adopting a half-light radius of $R_{\rm eff} = 0.68$ kpc (Bassa et al. 2017). In a pure rotational disk (e.g., the disk of a spiral galaxy), a comparable value is expected. The inferred mass is consistent with the stellar mass reported by Bassa et al. (2017) from a spectral energy distribution fit ($(1.3 \pm 0.4) \times 10^8 M_\odot$). This suggests that the velocity dispersion may be useful for the dynamical BH mass estimation. We also note that QRS 121102 is spatially associated with the Hα emission region.

Second, the M–σ relations could be less reliable at our velocity dispersion for two reasons. (1) Most reports derive the empirical M–σ relation based on a sample of more massive galaxies with larger stellar velocity dispersions. It is unclear how well the relation extends to lower velocity dispersions. (2) Even in the few reports that cover velocity dispersions down to 30 km s^{-1}, the M–σ relation is still less reliable due to the larger uncertainty in the empirical mass–luminosity (M–L) relation at the lower end. To derive the M–σ relation, the dynamical masses of the BHs were estimated using the virial relation, where the virial radius is either measured directly from reverberation mapping (e.g., Peterson 1993) or indirectly from the empirical M–L relation that was derived from the reverberation-mapped AGN. At the low-mass end, few AGN have been reverberation mapped, so an extrapolation of the M–L relation has to be made in the BH mass estimations, introducing extra uncertainty to the resulting M–σ relation. The M–σ relation might be flatter at the lower-mass end based on a few intermediate-mass BHs in the sample (e.g., Greene & Ho 2006), although the flattening is inconclusive without the reverberation mapping results of the lower-mass BHs.

We validate our BH mass estimation result by comparing to the empirical BH–galaxy mass correlation. Reines & Volonteri (2015) measured the correlation between galaxy stellar mass and BH mass based on a sample of 341 AGN host galaxies, including a subsample of dwarf galaxies (Reines et al. 2013). They found that $\log(M_{\rm BH}/M_\odot) = 7.45 + 1.05 \log(M_*/10^{11} M_\odot)$, with a scatter of 0.55 dex. A stellar mass of $10^8 M_\odot$ gives an AGN BH mass of $10^{4\sim5} M_\odot$ (1σ uncertainty assuming lognormal mass distribution), consistent with our BH mass estimation.

3.3. Keck/LRIS Low-resolution Spectral Analysis

Data were obtained with two long-slit orientations (shown in Figure 5). The LRIS data were bias subtracted, flattened, cosmic-ray removed, sky-line subtracted, and flux calibrated using the LPipe (Perley 2019). The LPipe wavelength calibration failed on the red side, since the arc lamp spectrum missed too many of the expected reference lines. We calibrated the wavelength manually by fitting the sky spectra to six isolated, bright sky lines. We then selected all nearby sources for which reliable spectra could be extracted: two sources near the host on slit 1 (S1, S2) and one on slit 2 (S3; Figure 5).

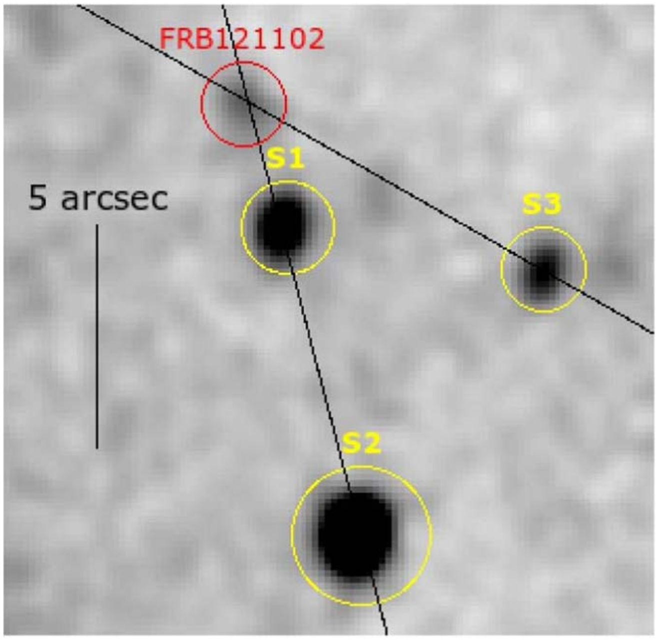

Figure 5. Locations of the host, slits, and sources in the low-resolution Keck/LRIS observation. The slit orientations are shown as black lines. Spectra were extracted for each of sources S1, S2, and S3, together with the QRS 121102 host. The background image is an LRIS R-band exposure, as presented in Tendulkar et al. (2017).

In this section, we evaluate whether or not the host and its nearby sources belong to the same galaxy group. The redshift of each spectrum was estimated as follows. The procedures were also tested on several SDSS spectra and yield results within 1% of the known redshift values.

1. Remove strong sky-line features and data near the boundaries of the wavelength coverage.
2. Interpolate and smooth the spectrum using a 1D Gaussian kernel ($\sigma = 3$ Å) to reduce random high-frequency noise. The kernel width was chosen such that it is narrower than the spectral line width at 8000 Å ($1\sigma \sim 5$ Å) for a typical galactic velocity dispersion of $\sim$200 km s^{-1} (e.g., Honma et al. 2012). Somewhat different kernel width choices (1, 3, and 5 Å) do not change the redshift results significantly.
3. Fit for the continuum and subtract from the spectrum. The fit was done using the *Astropy* package *specutils*, which removes spikes using a median filter and fits the spike-removed spectrum with a list of models using the Levenberg–Marquardt algorithm.
4. Extract a 60 Å long segment of spectrum centered at each typical galaxy absorption (or emission) line and stack them. We considered the following absorption lines, as they are near the visible wavelength at a redshift of $\sim$0–1: the Balmer series, Ca K&H (3934.777, 3969.588), the G band (4305.61), Mg (5176.7), Na (5895.6), and Ca [II] (8500.36, 8544.44, 8664.52). We ignored emission lines, since none of our sources show significant emission features. The segment width of 60 Å was chosen such that it was able to include at least the $\pm 5\sigma$ region of a spectral line broadened by a typical galactic velocity

   dispersion of 200 km s^{-1} (e.g., Honma et al. 2012) but not too wide to contain multiple lines.
5. Compare the amplitude of the stacked segment at a grid of trial redshift values. In this work, the best estimation occurs at the deepest valley, since we only considered absorption lines.

For S1, we find $z \approx 0.5796$ and inspect absorptive features at the wavelengths of Ca H+K, Mg, Hγ, and possibly the *G* band. For S2, we find $z \approx 0.4471$ and see absorptive features at the wavelengths of Ca K, the *G* band, Na, and potentially Hα. For S3, a few weak lines (Ca H, Mg, and Na) indicate that this source might be close to S2 in redshift, but we were unable to reach a conclusion due to the low S/N. We find no significant spectral feature at the expected wavelengths assuming that S3 was at the host redshift. None of the three sources is likely to be at the same redshift as the host of QRS 121102.

4. Discussion

4.1. Does QRS 121102 Scintillate?

4.1.1. Scattering Theory Predictions

Compact sources scintillate as their wavefronts propagate through an inhomogeneous ionized medium. Within the medium, fluctuations in the electron density lead to variations of the refractive index, which change the phase of the wave front. The fluctuations can be described by the phase structure function, defined as the phase difference of two points separated by a distance x:

$$D_{\varphi}(x) = \langle [\varphi(x + x_0) - \varphi(x)] \rangle_{x_0} \propto x^{\alpha}. \tag{2}$$

Here α is 5/3 for Kolmogorov turbulence (Armstrong et al. 1995). We adopt a Kolmogorov turbulence assumption in our calculations hereafter. When there are relative motions between the source, medium, and observer, the fluctuations cause temporal variations in the observed flux density.

One important scale of the scattering medium is r_0, the transverse radius (on the observer's plane) at which the phase changes by 1 rad ($D_{\phi}(r_0) = 1$) due to the ISM free electron inhomogeneity. r_0 can be related to σ_θ, the rms of the angle of arrival for a point source at distance D:

$$r_0 = \frac{\lambda}{\sqrt{2}\pi\sigma_\theta}, \tag{3}$$

$$\sigma_\theta^2 = \int_0^D dx\, \eta(x) \left(\frac{x}{D}\right)^2. \tag{4}$$

Here x is the source–observer axis, and $\eta(x)$ is the mean square of the scattering angle per unit length along the line of sight.

In general, $\eta(x)$ is determined by the wavelength λ, the SM, and the inner scale of the spatial power spectrum of the electron density fluctuation in the turbulent medium. The specific relation depends on the geometry and the power spectrum (e.g., see Cordes & Rickett 1998 for details).

For extragalactic sources, scattering is dominated by the Milky Way ISM, which can often be approximated as a thin scattering screen at a distance D from the observer (e.g., Romani et al. 1986). In Equation (4), the integration becomes a delta function at the distance of the galactic ISM screen.

Another characteristic scale of the scattering medium is the Fresnel scale (e.g., Narayan 1992),

$$\begin{aligned} r_{\mathrm{F}} &= \sqrt{\frac{\lambda D}{2\pi}} \\ &= 1.23 \times 10^9\ \mathrm{m} \left(\frac{D}{1\mathrm{kpc}}\right)^{1/2} \left(\frac{\nu}{1\mathrm{GHz}}\right)^{-1/2}, \end{aligned} \tag{5}$$

which is the transverse length (on the observer's plane) at which the phase of a wave front with wavelength λ changes by 1 rad due to the geometric path length difference, assuming that $D \gg \lambda$.

Based on the relation of these two scales (Equations (3) and (5)), scattering is divided into the weak regime ($r_0 \gg r_F$) and the strong regime ($r_0 \ll r_F$). The transitional frequency, ν_0, is defined as the frequency at which $r_0 \sim r_F$ for an extragalactic source. In the NE2001 electron density model (Cordes & Lazio 2002, 2003), the ν_0 for plane waves emitted by faraway sources is given by (adopted from Equation (17) of Cordes & Lazio 2002):

$$\nu_0 \approx 318\ \mathrm{GHz} \left(\xi \frac{r_0}{r_F}\right)^{10/17} \left(\frac{\mathrm{SM}}{1\ \mathrm{kpc\ m^{-20/3}}}\right)^{6/17} \left(\frac{D_{\mathrm{eff}}}{1\ \mathrm{kpc}}\right)^{5/17}. \tag{6}$$

Here $\xi = 1/\sqrt{2\pi}$ is the Fresnel scale definition factor, $\mathrm{SM} = \int_0^D \mathrm{ds}\ \mathrm{C}_{n_e}^2(\mathrm{s})$ is the SM, and $C_{n_e}^2$ describes the strength of the free electron density fluctuations along the line of sight. We adopt an SM of 0.00614 kpc $\mathrm{m}^{-20/3}$ based on the NE2001 model along the line of sight, and

$$D_{\mathrm{eff}} = \frac{\int_0^D ds\ s\ C_{n_e}^2}{\int_0^D ds\ C_{n_e}^2}$$

is the effective path length through the medium. We find $D_{\mathrm{eff}} \approx 2$ kpc, as calculated using NE2001 by $D(\mathrm{SM} - \mathrm{SM}_\tau/6 - \mathrm{SM}_\theta/3)/\mathrm{SM}$, where we use $D = 30$ kpc for extragalactic sources, $\mathrm{SM}_\tau = \int \mathrm{ds}(\mathrm{s}/\mathrm{D})(1 - \mathrm{s}/\mathrm{D})\mathrm{C}_{n_e}^2 \approx 0.0023\ \mathrm{kpc\ m^{-20/3}}$, and $\mathrm{SM}_\theta = \int \mathrm{ds}(1 - \mathrm{s}/\mathrm{D})\mathrm{C}_{n_e}^2 \approx 0.016\ \mathrm{kpc\ m^{-20/3}}$. We estimate that $\nu_0 = 38$ GHz along the line of sight of QRS 121102 ($l \approx 175°$, $b \approx -0\overset{\circ}{.}2$). Our observations were taken at frequencies (12–26 GHz) below ν_0, so they all belong to the strong scattering regime.

In the strong scattering regime, there are two main types of scintillation behaviors: refractive and diffractive. We summarize the predicted scintillation behaviors below based on Romani et al. (1986) and Walker (1998).

Refractive scintillation is caused by large-scale ($\gg r_F$) ISM inhomogeneities. The observed flux density variability is slow and broadband. For Kolmogorov turbulence, the angular radius of the apparent scattering disk at a frequency ν is (Walker 1998)

$$\begin{aligned} \theta_{\mathrm{r}} &= \theta_{\mathrm{F0}} \left(\frac{\nu_0}{\nu}\right)^{11/5} \\ &= 1.32\ \mu\mathrm{as} \left(\frac{D}{1\mathrm{kpc}}\right)^{1/2} \left(\frac{\nu_0}{\nu}\right)^{11/5}. \end{aligned} \tag{7}$$

Table 4
Predicted Galactic Refractive Scintillation Properties of QRS 121102[a]

Band (ν_c)	m_p (%)	t_r (hr)	θ_r[b] (μas)
K (22 GHz)	73	∼7	4
U (15 GHz)	59	∼16	10

Note.
[a] Assuming a point source and Kolmogorov turbulence.
[b] Assuming a nominal distance between the scattering screen and the observer to be 1 kpc.

Here θ_{F0} is the angular size of the first Fresnel zone at the transitional frequency ν_0:

$$\theta_{F0} = \sqrt{\frac{c}{2\pi\nu_0 D}} = 8.11\ \mu\mathrm{as}\left(\frac{D}{1\ \mathrm{kpc}}\right)^{1/2}\left(\frac{\nu_0}{1\ \mathrm{GHz}}\right)^{-1/2}. \tag{8}$$

The observed flux density of a compact source smaller than θ_r varies on a refractive timescale of (Walker 1998) $t_r \sim 2r_r/v = (2r_{F_0}/v)(\nu_0/\nu)^{11/5} \sim 2\ \mathrm{hr}(\nu_0/\nu)^{11/5}$. Here we assume a typical relative transverse velocity of 50 km s^{-1} (Rickett et al. 1995) and an ISM scattering screen distance of 1 kpc from the observer, and we use the diameter of the apparent scattering disk at a frequency ν as the length scale. In this work, the modulation index is defined as the weighted rms fractional variation:

$$m_p = \frac{1}{\langle f\rangle}\sqrt{\frac{\sum_i w_i(f_i - \langle f\rangle)^2}{\sum_i w_i}}. \tag{9}$$

Here f_i is the flux density of the ith epoch, $w_i = 1/\sigma_{f_i}^2$ is the weight calculated from the measurement uncertainty σ_{f_i}, and $\langle f\rangle$ is the weighted mean flux density. The modulation index of a source smaller than θ_r is given by (Walker 1998)

$$m_p = \left(\frac{\nu}{\nu_0}\right)^{17/30}. \tag{10}$$

When the point-source approximation fails ($\theta_s > \theta_r$, where θ_s is the source angular radius), the modulation index reduces as $m = m_p(\theta_r/\theta_s)^{7/6}$, and the variability timescale increases as $t = t_r(\theta_s/\theta_r)$.

Table 4 lists the predicted θ_r (Equation (7)), t_r, and m_p (Equation (10)) using the central frequency of each band and assuming a point source. We do not predict the substantially larger effects of diffractive scintillation because, as will be seen below, we observe significantly less modulation than expected due to refractive scintillation alone. We calculate θ_r (Equations (7) and (8)) using a distance D ranging from 100 pc to 10 kpc (Figure 6) and list the θ_r corresponding to a nominal distance of 1 kpc (∼galactic scale height) in Table 4. For scattering media dominated by a steeper fluctuation spectrum, the expected values of m_p, t_r, and θ_r would be greater (Armstrong et al. 1995).

In contrast, diffractive scintillation is produced by interference effects between light rays passing through small-scale ($\ll r_F$) ISM inhomogeneities. The variations are fast ($t_d \sim 2(\nu/\nu_0)^{6/5} \sim 5$ hr at $\nu = 18$ GHz) and narrowband ($\Delta\nu \approx \nu(\nu/\nu_0)^{17/5} \approx 1$ GHz at $\nu = 18$ GHz). This is beyond the scope of this paper.

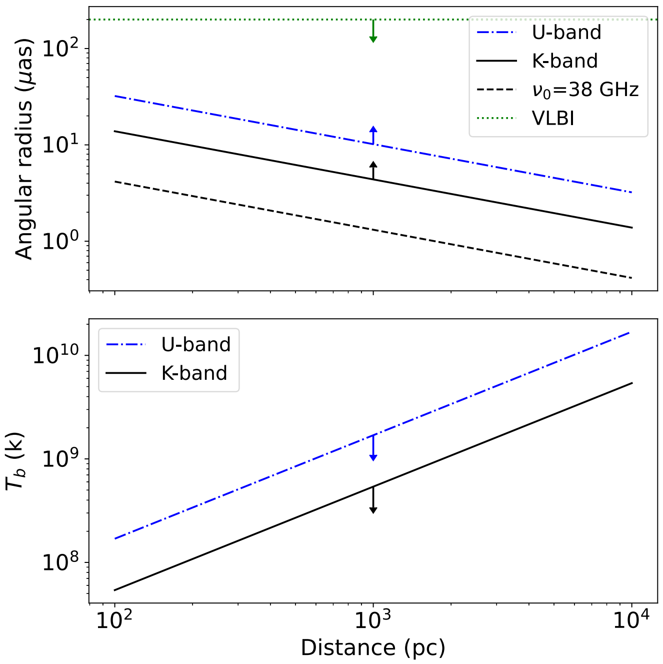

Figure 6. Implication from the lack of refractive scintillation modulation assuming a range of distances between the scattering screen and the observer. Upper panel: source radius lower limits in the Ku (dashed–dotted blue line) and K (solid black line) bands, the scattering disk radius at the transitional frequency ν_0, as well as the source radius upper limit from the unresolved VLBI image at 5 GHz. Lower panel: brightness temperature upper limits using the emission region size lower limit inferred from the Ku band ($\theta_r \gtrsim 10\ \mu$as) and the weighted average flux densities measured in the Ku (dashed blue line) and K (solid black line) bands.

Table 5
VLA Flux Density Modulation Indices Results and Statistical Tests

Data (Band)	$m_p{}'$ (Observed) (%)	$\chi^2_{\min}$ (dof)	Constant $P(\geqslant\chi^2_{\min};\nu)$ (%)	Refractive Scintillation $P(\leqslant\chi^2_\nu; m_p)$ (%)
f3/f2[a] (K)	(19.3 ± 7.1)	5.8 (2)	5.6	∼9
f3/f2 (U)	(13.3 ± 4.8)	10.9 (3)	1.2	∼3
f3[b] (K)	(30.2 ± 5.8)	13.9 (2)	10^{-3}	∼20
f3 (U)	(26.1 ± 4.4)	48.5 (3)	10^{-10}	∼23

Notes.
[a] The flux density measurements of QRS 121102 divided by those of J0518+3306 and then normalized to an average of unity.
[b] The normalized flux density measurements of QRS 121102.

4.1.2. Comparison between the Flux Density Measurements and Predictions

In the following analyses, we analyze two types of flux density measurements in each band.

1. The normalized flux density measurements of QRS 121102 (f3 in Table 5).
2. The flux density measurements of QRS 121102 divided by those of J0518+3306 and then normalized (f3/f2 in Table 5). The scaling is justified for two reasons. (1) The phase calibrators J0518+3306 (and J0518+3306) are not

expected to scintillate, since the constraints on their angular radii and the observed flux densities would require a brightness temperature exceeding the inverse Compton catastrophe threshold, $\gtrsim 10^{12}$ K (and $\gtrsim 10^{13}$ K), assuming a scattering screen at 1 kpc. (2) The variations are unlikely to be intrinsic due to the strong correlations and the short variation timescale, as explained in Section 3.1.

We calculate the modulation indices of the above four sets of flux density measurements (Table 5, second column) and find each of them to be more than 5σ lower than the predictions (error bar calculated from the statistical errors in the flux density measurements), though our observation spacings are longer than the predicted refractive timescale (Table 4). To conclude the comparison, we perform χ^2 tests for two hypotheses.

1. The flux density is constant.
2. The flux density measurements are drawn from a Gaussian distribution whose standard deviation is equal to the scattering theory prediction (Table 4, Section 4.1.1). A Gaussian distribution is used here to provide a conservative test, though galactic scattering has been observed to modulate intensity with one-sided exponential functions (e.g., Cordes 2002).

We test the first hypothesis by fitting our measurements in each band with their weighted average and calculating the χ^2:

$$\chi^2 = \sum_i \frac{(f_i - \langle f \rangle_w)^2}{\sigma_{f_i}^2}. \tag{11}$$

Here $\langle f \rangle_w$, f_i, and σ_{f_i} are the weighted average flux density, the ith epoch flux density, and its measurement error, respectively. For example, in the K band, the best-fit result of f3/f2 has a $\chi^2_{\min}$ of 5.8 and a degree of freedom (dof) of 2, yielding a one-sided p-value of 5.6% for obtaining a $\chi^2_{\min}$ that is greater than or equal to our observation if the flux density were constant. Other results are listed in Table 5. In both bands, the constant flux density hypothesis is questionable using the f3/f2 light curve and is rejected to a level of at least 10^{-3} using the f3 light curve.

We test the second hypothesis by simulating 10^5 light curves for both bands, each with the same number of measurements and the same fractional uncertainties as our observations. For each light curve, the flux densities are drawn from the absolute values of a Gaussian distribution centered at unity and with a standard deviation of $m_p\sqrt{n/(n-1)}$, where m_p is the expected modulation index, and n is the number of measurements. We calculate the χ^2_ν for each light curve and compare the smoothed distribution with our observations in each band. For example, using f3/f2 in the Ku band, ~3% of the simulated light curves have χ_ν values lower than or equal to our observation (2.9), questioning the second hypothesis. In both bands, the scintillation variability hypothesis is doubtful using the f3/f2 data.

4.1.3. Implications

We have found it questionable that our observation is consistent with refractive scintillation predictions for a point-like source. We will discuss the implications of the absence of refractive scintillation modulation in our observations.

First, scintillation variations will be smeared out if the angular size of the source is greater than that of the scattering disk. The lack of modulation implies a lower limit to the physical size of the source in each band (Figure 6). Here the scattering disk angular size lower limit is calculated assuming a range of distances from 100 pc to 10 kpc between the scattering screen and the observer. The physical size limit of the source is obtained using the angular size limit and the host redshift ($z = 0.19273$). In the Ku band, the scattering disk radius is 10 μas (Table 4) assuming a scattering screen distance of 1 kpc (~galactic scale height), corresponding to a physical radius of $R \gtrsim 10^{17}$ cm (0.03 pc) at the host redshift. This, together with the VLBI resolution at 5 GHz, limits the emission radius to between $\sim 10^{17}$ and $\sim 10^{18}$ cm. Alternatively, a rough estimation of the source radius could be made using the measured modulation index. When the angular radius of the source is larger than that of the refractive scattering disk, the variability will reduce, and the source radius is given by $\theta_s \approx \theta_r (m_p/m_p{}')^{6/7}$, where m_p is the expected scintillation modulation index, $m_p{}'$ is the observed modulation index, and θ_r is the refractive scintillation disk angular radius. This gives a source radius of 14 μas (1.4×10^{17} cm) in the K band and 36 μas (3.7×10^{17} cm) in the Ku band (using the host redshift and assuming a scattering screen at 1 kpc), within the above constraints of 10^{17-18} cm.

In addition, the constraint on source size rules out the scenario that the flux density modulation is intrinsic. The flux density varies significantly within a week in the Ku band (e.g., epochs 3, 4, and 5). If the modulations were intrinsic, the source radius would be $R \lesssim (1/2) \cdot (7\,\text{days}) \cdot \mathrm{c} \sim 10^{14}$ cm, 3 orders of magnitude below the scintillation size limit. The source would also have scintillated more if the fast variations were intrinsic.

Moreover, the brightness temperature of the source can be constrained by its size limit and flux density measurement. Brightness temperature provides clues to the radio emission process. For example, a brightness temperature above 10^5 K may rule out star-forming galaxies (e.g., Condon 1992), and a brightness temperature above 10^{12} K requires coherent processes or relativistic boosting (e.g., Rybicki & Lightman 1979). The brightness temperature is given by

$$T_{\mathrm{b}} \lesssim \frac{fc^2}{2\pi\theta^2_{\mathrm{r,15GHz}} k_{\mathrm{b}} \nu^2}. \tag{12}$$

Here $\theta_{\mathrm{r,15\,GHz}}$ is the radius lower limit implied by the lack of scintillation modulation in the Ku band, and ν is the frequency at which the flux density f is measured. Assuming a scattering screen distance of 1 kpc (Table 6), we find $T_{\mathrm{b}} \lesssim 5 \times 10^8$ K using our average flux density measured in the K band ($\nu_c = 22$ GHz, $\langle f_\nu \rangle \approx 61.3 \pm 5.0$ μJy, weighted by the statistical errors in the flux density measurements) and $T_{\mathrm{b}} \lesssim 2 \times 10^9$ K using the weighted average flux density measured in the Ku band ($\nu_c = 15$ GHz, $\langle f_\nu \rangle \approx 61.3 \pm 5.0$ μJy). A more complete result assuming a range of scattering screen distances is shown in Figure 6.

4.2. Optical

4.2.1. Implications of Constraint on Potential Supermassive BH Mass

We have estimated the mass of the potential supermassive BH to be $10^{4-5} M_\odot$ using the velocity dispersion measured from the Hα emission line width (Section 3.2). We will test the

Table 6
Implications of the Lack of Refractive Scintillation

Observation	$\langle f_\nu \rangle$ [a] (μJy)	Radio Luminosity[b] (erg s^{-1})	Radius[c] (cm)	$T_{\rm b}$[c] (K)
VLA *K* band (22 GHz)	61.3 ± 5.0	1.5×10^{39}	$\gtrsim 4 \times 10^{16}$	$\lesssim 5 \times 10^{8}$
VLA *Ku* band (15 GHz)	89.4 ± 3.4	1.5×10^{39}	$\gtrsim 10^{17}$	$\lesssim 2 \times 10^{9}$

Notes.
[a] Weighted average flux density.
[b] Isotropic luminosity $L \approx \nu_c \langle f_\nu \rangle 4\pi D_L^2$, where ν_c is the band central frequency.
[c] Assuming a nominal distance of 1 kpc between the scattering screen and the observer.

AGN hypothesis by comparing its mass, radio luminosity, and X-ray luminosity with the AGN population.

The radio luminosity of QRS 121102 is several orders of magnitude higher than expected given $M_{\rm BH} \approx 10^{4-5} M_\odot$, based on results from a large sample of AGN with higher BH masses (Lacy et al. 2001). However, it may not be rare in a sample of bright radio emissions detected in dwarf galaxies at intermediate redshifts (Mezcua et al. 2019) and is only slightly brighter than those detected in some nearby dwarf galaxies (Reines et al. 2020). For the general AGN population, the BH mass ($M_{\rm BH}$), radio luminosity ($L_{5\,\rm GHz}$), and ratio of bolometric luminosity to the Eddington limit ($L/L_{\rm Edd}$) has been reported to be correlated. For example, Lacy et al. (2001) measured a relation based on a sample of 60 AGN with BH masses of $10^{6.5-10} M_\odot$: $\log_{10}(L_{5\,\rm GHz}) = 1.9 \log_{10}(M_{\rm BH}/M_\odot) + x \log_{10}(L/L_{\rm Edd}) + 7.9$ (with a scatter of 1.1 dex), where $L_{5\,\rm GHz}$ is in units of W Hz^{-1} sr^{-1}; $x \approx 1$ for a typical $(L/L_{\rm Edd})$ of 0.1; and $x \approx 0.3$ for a low $(L/L_{\rm Edd})$ of 10^{-5}. The specific radio luminosity of QRS 121102 is $L_{5\,\rm GHz} \approx 10^{21.2}$ W Hz^{-1} sr^{-1}, as calculated using the host redshift and the flux density of $\approx 200\,\mu$Jy at 3 and 6 GHz (Chatterjee et al. 2017). This is 3 orders of magnitude greater than calculated from the relation (scatter included) even if $L/L_{\rm Edd} = 100\%$ and $M_{\rm BH} = 10^5 M_\odot$. However, we note that the relation reported in Lacy et al. (2001) is derived from a sample of more massive BHs ($10^{6.5-10} M_\odot$).

It is intriguing that the radio luminosity of QRS 121102 is consistent with a sample of bright radio emissions detected in dwarf galaxies at intermediate redshifts (Mezcua et al. 2019). The specific radio luminosity of QRS 121102 at 3 GHz is $L_{3\,\rm GHz} \sim 2.3 \times 10^{22}$ W Hz^{-1}, as calculated using the host redshift and flux density at 3 GHz ($206 \pm 17\,\mu$Jy; Chatterjee et al. 2017). This lies within the broad luminosity range ($L_{3\,\rm GHz} \approx 10^{21.5-24.2}$ W Hz^{-1}) observed in a sample of 35 dwarf galaxies ($10^7 < M_* < 10^{9.5}$) at intermediate redshifts (0.13–3.4) hosting compact radio sources from the VLA-COSMOS 3 GHz Large Project catalog (Mezcua et al. 2019). These sources are suspected to be AGN mainly because they are significantly more luminous ($\geqslant 2\sigma$) than expected from star formation processes. In particular, a few objects in their sample show similar radio luminosities, host stellar masses, BH mass estimations, and redshifts with QRS 121102, although the constraints on their X-ray luminosities are weaker (Tables 1 and 2 of Mezcua et al. 2019). Similarly, the specific luminosity at 10 GHz ($\sim 1.9 \times 10^{22}$ W Hz^{-1}) is only slightly above the observed range ($10^{18.5-22}$ W Hz^{-1}) from 13 nearby ($z < 0.055$) dwarf galaxies hosting bright radio sources that are too bright to be star formation processes or supernova remnants (Reines et al. 2020). We suggest that the nature of several of these radio sources, including QRS 121102, remains uncertain (e.g., Law et al. 2022).[2]

In addition, we estimate the minimum average radio luminosity of QRS 121102 during its past life span and find it uncomfortably high given the constraints on the X-ray luminosity. We assume possible source radii of 10^{17} cm (the lower limit from this work) and 10^{18} cm (the upper limit from the previous VLBI observation; Marcote et al. 2017) and calculate the minimum energy (equipartition energy) based on Section 2.3 of Vedantham & Ravi (2019). Assuming a power-law electron energy distribution of index −1.5 (to enable direct comparison with Vedantham & Ravi 2019 and account for the flat spectrum), the minimum total energies required to power a synchrotron source with the observed radio luminosity at these two size limits are $E_{\rm q} \approx 10^{48.9}$ ergs ($B_{\rm eq} \approx 27$ mG) and $\approx 10^{50.2}$ ergs ($B_{\rm eq} \approx 190$ mG), respectively (e.g., Chapter 5 of Condon & Ransom 2016). Adopting a conservative expansion speed of $\sim 0.01\,c$ (Vedantham & Ravi 2019), the average radio luminosity during its past life span would be 2×10^{40} erg s^{-1} (5×10^{40} erg s^{-1}), about 0.2% (0.5%) of the Eddington limit for a $10^5 M_\odot$ BH. This is uncomfortably high, accounting for typical amounts (∼10%) of energy deposited into relativistic electrons, given the upper limit on X-ray emission of 4% of the Eddington limit for a $10^5 M_\odot$ BH (Chatterjee et al. 2017).

The radio and X-ray observations of QRS 121102 can also be compared with the radio/X-ray luminosity correlation in accreting BH systems (e.g., Hannikainen et al. 1998). In particular, the AGN BH mass has been found to be correlated with its radio and X-ray luminosity (e.g., Merloni et al. 2003; Falcke et al. 2004). A recent report based on a sample of 30 AGN with independent dynamical mass measurements shows that $\log(M/10^8\,M_\odot) = 0.55 + 1.09 \log(L_R/10^{38} {\rm erg\,s^{-1}}) - 0.59 \log(L_X/10^{40} {\rm erg\,s^{-1}})$ (Gültekin et al. 2019), with a 1σ scatter of 1 dex assuming a lognormal mass distribution. Here L_R and L_x are the luminosity at 5 GHz and 2–10 keV, respectively, observed within close epochs ($\Delta t \lesssim 2 + M/10^6 M_\odot$ days). We adopt a 5 GHz flux density of $f_R \approx 5\,{\rm GHz} \cdot 200\,\mu{\rm Jy} \sim 10^{-17} {\rm erg\,s^{-1}\,cm^{-2}}$ measured by VLA and an X-ray flux upper limit of $f_x \lesssim 5 \times 10^{-15} {\rm erg\,s^{-1}\,cm^{-2}}$ inferred from the nondetection in the XMM-Newton and Chandra images (Chatterjee et al. 2017). We convert the flux density to isotropic luminosity using the host redshift and have $L_R \approx 10^{39}$ and $L_x \lesssim 5 \times 10^{37} {\rm erg\,s^{-1}}$, giving a BH mass of $\sim 10^{11} M_\odot$, 6–7 orders of magnitude greater than our measurement. Therefore, the persistent radio source does not follow the AGN BH mass–luminosity relation measured in Gültekin et al. (2019).

4.2.2. AGN in an Isolated Dwarf Galaxy

A fraction (8%–32%) of supermassive BHs have been estimated to reside within high-mass ultracompact dwarf galaxies, suggesting that some of those galaxies could be the stripped cores of larger galaxies through tidal interactions with their companions (Voggel et al. 2019). We find that this scenario is not supported for QRS 121102 for two reasons. First, the low BH mass estimated from the gas velocity dispersion is consistent with a typical dwarf galaxy instead of a

---

[2] Although see Molina et al. (2021) for an example of an unambiguous AGN in a dwarf galaxy.

more massive galaxy (Section 3.2). Second, members of the same galaxy group are expected to be associated with QRS 121102 if the host has been dynamically stripped by nearby companions. From the low-resolution LRIS spectra, we found that the three nearby bright sources are likely to have different redshift values from the host (Section 3.3).

We extend this argument by searching the PanSTARRS catalog for potential companions that are likely to belong to the same galaxy group. We search the PanSTARRS catalog for sources within 5′ (∼1 Mpc, the virial radius of a galaxy group with a typical mass of $\sim 10^{13}\,M_\odot$ and velocity of 200 km s^{-1}) that have consistent photometric redshift measurements with the host. One object (PSO J082.9850+33.0967) was found at 3′ from QRS 121102, but it was only detected in a stacked image and has no valid magnitude measurement available in the catalog. Another object (PSO J082.9961+33.0895) was ignored due to the large uncertainty in its photometric redshift (0.20 ± 0.18). We find no promising group member candidate from the PanSTARRS catalog. Moreover, we compare the PanSTARRS galaxy number density within this area with the galaxy number density calculated from the deep *VRI* images in the *R* band produced by the Keck Telescope (Smail et al. 1995). In that work, they estimated a galaxy number density of $\approx 7 \times 10^5$ deg^{-2} with a magnitude range of $20.5 \lesssim m_R \lesssim 27.2$. In the PanSTARRS DS1 catalog, 2705 objects are found within a radius of 5′ around QRS 121102, and 30 of them are classified as galaxies above a confidence level of 90% (Tachibana & Miller 2018). The limiting magnitude of PanSTARRS is $m_r \approx 23.2$, six times shallower than that of the deep *VRI* images, predicting ≈60 galaxies within the searched area at a limiting magnitude of 23.2. The galaxy number density near QRS 121102 is not overdense compared to an average sky region. We find no evidence that the host belongs to a galaxy group.

4.3. What Else Could the Source Be?

We have found that QRS 121102 is unlikely to be an AGN based on the low inferred BH mass ($\lesssim 10^{4-5} M_\odot$), high radio-to-X-ray luminosity ratio, and absence of companions from the same galaxy group. In this section, we discuss other possible sources for the compact persistent radio emission.

The size of the persistent radio emission could be explained by an isolated young neutron star with luminous synchrotron emission produced in a PWN, or plerion. The pulsar wind forms a terminal shock at a radius where the wind momentum flux and confining pressure reach a balance and forms a PWN further out. The shock radius is given by $r_w = \sqrt{\dot{E}/(4\pi\eta c p)}$ (Slane 2005), where $\dot{E}$ is the pulsar energy injection rate into the wind, η is the fraction of area covered by the wind, c is the speed of light, and p is the confining pressure outside the shock and is proportional to the electron number density n_e for a medium with the same components. The relation gives a radius of ∼0.1 pc for a canonical isolated radio pulsar and is confirmed to be $\approx 3 \times 10^{17}$ cm from the X-ray images of the Crab Nebula (Weisskopf et al. 2000). For the Crab pulsar, the spin-down energy rate is $\dot{E} \sim 4.5 \times 10^{38}$ ergs s^{-1} (Staelin & Reifenstein 1968), and the confining pressure outside the shock is proportional to the density of the medium, which can be approximated as a typical ISM ($n_e \sim 10^{-1}$–10^{-2} cm^{-3}; e.g., Draine 2011). In comparison, the energy ejection rate of QRS 121102 by the flares and wind into the surrounding medium is estimated to be $\dot{E} \sim 10^{39}$–10^{40} ergs s^{-1} (Figure 5 of Margalit et al. 2020), and the medium ahead of the termination shock is likely denser than a typical ISM, as indicated from the high RM of QRS 121102 (Michilli et al. 2018).

One example of the PWN emission model that produces the observed radio luminosities and the size of QRS 121102 is presented in Margalit & Metzger (2018), where the authors explained the persistent emission using a concordance FRB model. On a large scale ($\sim 10^{15}$ cm; Equation (4) of Metzger et al. 2019), the train of ion–electron shells merges into a steady wind and feeds into a nebula via a terminal shock, which heats up electrons in the nebula and produces the persistent synchrotron radio source. Based on the lack of self-absorption features down to 6.0 GHz in the spectrum of the persistent source (Chatterjee et al. 2017), Margalit & Metzger (2018) estimated that the emission region's radius is $R \gtrsim 0.46 \times 10^{17}$ cm adopting the observed luminosity at 6 GHz. Moreover, Resmi et al. (2021) reported the lack of self-absorption down to 400 MHz in their GMRT observations. Using their flux density measurement at 400 MHz and the scaling relation $R \propto L_{\nu,\mathrm{obs}}^{4/11} \nu_{\mathrm{obs}}^{-10/11}$ (Equation (21) in Margalit & Metzger 2018), we find that $R \gtrsim 5.4 \times 10^{17}$ cm. This emission size is consistent with the constraint implied by the lack of refractive scintillation in the *Ku* band.

Among the more unique features of QRS 121102 is its unusually flat radio spectrum at gigahertz frequencies (Chatterjee et al. 2017). As we have noted, several examples of compact radio sources of similar luminosities exist in dwarf galaxies. Indeed, two recent discoveries of transient radio sources not associated with BHs also reached similar radio luminosities. The first, FIRST J141918.9+394036, had a peak radio luminosity of 2×10^{29} erg s^{-1} Hz^{-1} at 1.4 GHz and is hosted by a star-forming dwarf galaxy (Law et al. 2018). FIRST J141918.9+394036 is most likely the afterglow of an off-axis LGRB (Mooley et al. 2022). The second, VT J121001+495647, had a peak radio luminosity of 1.5×10^{29} erg s^{-1} Hz^{-1} at 5 GHz, was associated with a star-forming region, and was ascribed to interaction with a dense circumstellar medium ejected through binary interaction (Dong et al. 2021). In both cases, however, classical synchrotron spectral shapes were observed together with secular time evolution, unlike in the case of QRS 121102. We urge continued wideband monitoring of QRS 121102, together with a more detailed evaluation of potential empirical analogs.

Finally, we rule out a few other possible origins of QRS 121102 based on our observations. First, the source cannot be a supernova remnant (SNR) due to its high luminosity. We have calculated the specific luminosity of QRS 121102 at 3 and 10 GHz as $L_\nu \sim 10^{22}$ W Hz^{-1}. Ulvestad (2009) and Varenius et al. (2019) recently reported the radio luminosities (5 GHz and 8.4 GHz) of 102 SNRs in the merging galaxies Arp 220 and Arp 229. The brightest SNR in the sample is $L_\nu < 10^{21}$ W Hz^{-1}, over 1 order of magnitude lower than QRS 121102. Moreover, the luminosity is inconsistent with the star formation rate (SFR) of the host galaxy if the source were an SNR(s). The brightest SNR and the SFR of a galaxy have been reported to be related (Chomiuk & Wilcots 2009) as $L_{1.4}^{\max} = 95^{+31}_{-23}\,\mathrm{SFR}^{0.98\pm0.12}$, where $L_{1.4}^{\max}$ is in units of 10^{24} erg s^{-1} Hz^{-1}, and SFR is in $M_\odot$ yr^{-1}. Adopting the SFR upper limit of 0.4 $M_\odot$ yr^{-1} based on the host Hα emission flux (Tendulkar et al. 2017), the brightest SNR in the host would be $L_{1.4}^{\max} \approx 10^{18.6}$ W Hz^{-1}, over 3 orders of magnitude lower than QRS 121102. The persistent source is too bright to be an SNR. Second, the source is too bright for an LGRB radio afterglow. Adopting a typical LGRB peak radio luminosity of $L_{\nu,8.5\,\mathrm{GHz}} \sim 2 \times 10^{31}$ erg^{-1} s^{-1} Hz^{-1} and a decay rate of $\propto t^{-2}$ from day 10 after the GRB (e.g., Berger et al. 2003), the radio luminosity would have reached the level of QRS 121102 ($L_{\nu,10\,\mathrm{GHz}} \approx 2 \times 10^{29}$ erg^{-1} s^{-1}Hz^{-1}) within 3 weeks, while the radio luminosity of QRS 121102 would have been nearly constant below 10 GHz for years (e.g., Tendulkar et al. 2017; Resmi et al. 2021).

5. Conclusion

In this work, we investigated the origin of the persistent radio source, QRS 121102, associated with FRB 121102. We present new VLA monitoring data (12–26 GHz) and new spectra from Keck/LRIS. The main results are summarized as follows.

1. We constrained the emission radius to be 10^{17-18} cm based on the low level of scintillation variability in our VLA observations and the previous VLBI observation. A few compact radio sources (e.g., AGN, PWNs, very young SNRs, and GRB afterglows) could fall into these size limits. Most interpretations, with the exception of an AGN, would have been in tension with a converse finding of significant scintillation in QRS 121102.
2. To further investigate the hypothesis that the source is an AGN, we roughly constrained the mass of the potential BH to be $\lesssim 10^{4-5} M_{\odot}$ using the Hα velocity dispersion. The radio luminosity ($L_{\nu} \sim 2 \times 10^{22}$ W Hz^{-1} from 400 MHz to 10 GHz) is possibly too high at this BH mass compared to the general AGN population, although similarly bright radio emissions have been reported in several dwarf galaxies. The source is also unlikely to be an AGN because it is too faint in the X-ray for its low BH mass and bright radio emission.
3. A significant fraction of dwarf galaxies hosting supermassive BHs may be the stripped cores of massive galaxies during tidal interactions with their nearby companion(s). From our LRIS spectra and the Pan-STARRS catalog, we found no promising companion galaxy near the host to support an environment for a tidal stripping event history.
4. We briefly discussed possible origins other than AGN. QRS 121102 is too luminous in the radio band to be an SNR and too old to be a typical GRB afterglow. The isolated young neutron star models for FRBs might be able to account for both the size and the luminosity of the persistent source as synchrotron emission produced in the PWN (e.g., Metzger et al. 2019).

In conclusion, the persistent radio emission associated with QRS 121102 is likely not an AGN, and its nature remains interesting for FRB emission models involving extreme neutron stars.

Acknowledgments

The authors thank Dr. Casey J. Law for VLA imaging and visualization tips and the catalog querying code *psquery*. We also thank Dr. Casey J. Law and Dr. Liam D. Connor for helpful discussions on PRS and the unknown radio emissions in dwarf galaxies. We thank staff members at the CASA help desk, Dillon Dong, and Nitika Yadlapalli for CASA tips. This material is based upon work supported by the National Science Foundation under grant No. AST-1836018.

ORCID iDs

Ge Chen https://orcid.org/0000-0003-2867-4544
Vikram Ravi https://orcid.org/0000-0002-7252-5485
Gregg W. Hallinan https://orcid.org/0000-0002-7083-4049

References

Armstrong, J. W., Rickett, B. J., & Spangler, S. R. 1995, ApJ, 443, 209
Baldwin, J. A., Phillips, M. M., & Terlevich, R. 1981, PASP, 93, 5
Bassa, C. G., Tendulkar, S. P., Adams, E. A. K., et al. 2017, ApJL, 843, L8
Berger, E., Kulkarni, S. R., Pooley, G., et al. 2003, Natur, 426, 154
Briggs, D. S. 1995, AAS Meeting Abstracts, 187, 112.02
Chatterjee, S., Law, C. J., Wharton, R. S., et al. 2017, Natur, 541, 58
CHIME/FRB Collaboration, Amiri, M., Andersen, B. C., et al. 2021, ApJS, 257, 59
Chomiuk, L., & Wilcots, E. M. 2009, ApJ, 703, 370
Condon, J. J. 1992, ARA&A, 30, 575
Condon, J. J., & Ransom, S. M. 2016, Essential Radio Astronomy (Princeton, NJ: Princeton Univ. Press)
Cordes, J. M. 2002, in ASP Conf. Ser. 278, Single-Dish Radio Astronomy: Techniques and Applications, ed. S. Stanimirovic et al. (San Francisco, CA: ASP), 227
Cordes, J. M., & Lazio, T. J. W. 2002, arXiv:astro-ph/0207156
Cordes, J. M., & Lazio, T. J. W. 2003, arXiv:astro-ph/0301598
Cordes, J. M., & Rickett, B. J. 1998, ApJ, 507, 846
Cruces, M., Spitler, L. G., Scholz, P., et al. 2021, MNRAS, 500, 448
Dong, D. Z., Hallinan, G., Nakar, E., et al. 2021, Sci, 373, 1125
Draine, B. T. 2011, Physics of the Interstellar and Intergalactic Medium (Princeton, NJ: Princeton Univ. Press)
Falcke, H., Körding, E., & Markoff, S. 2004, A&A, 414, 895
Ferrarese, L., & Ford, H. 2005, SSRv, 116, 523
Franzen, T. M. O., Davies, M. L., Davies, R. D., et al. 2009, MNRAS, 400, 995
Greene, J. E., & Ho, L. C. 2006, ApJL, 641, L21
Gültekin, K., King, A. L., Cackett, E. M., et al. 2019, ApJ, 871, 80
Gültekin, K., Richstone, D. O., Gebhardt, K., et al. 2009, ApJ, 698, 198
Hannikainen, D. C., Hunstead, R. W., Campbell-Wilson, D., & Sood, R. K. 1998, A&A, 337, 460
Ho, L. C., Sarzi, M., Rix, H.-W., et al. 2002, PASP, 114, 137
Honma, M., Nagayama, T., Ando, K., et al. 2012, PASJ, 64, 136
Kokubo, M., Mitsuda, K., Sugai, H., et al. 2017, ApJ, 844, 95
Lacy, M., Laurent-Muehleisen, S. A., Ridgway, S. E., Becker, R. H., & White, R. L. 2001, ApJL, 551, L17
Law, C. J., Connor, L., & Aggarwal, K. 2022, ApJ, 927, 55
Law, C. J., Gaensler, B. M., Metzger, B. D., Ofek, E. O., & Sironi, L. 2018, ApJL, 866, L22
Lorimer, D. R., Bailes, M., McLaughlin, M. A., Narkevic, D. J., & Crawford, F. 2007, Sci, 318, 777
Marcote, B., Paragi, Z., Hessels, J. W. T., et al. 2017, ApJL, 834, L8
Margalit, B., & Metzger, B. D. 2018, ApJL, 868, L4
Margalit, B., Metzger, B. D., & Sironi, L. 2020, MNRAS, 494, 4627
McConnell, N. J., & Ma, C.-P. 2013, ApJ, 764, 184
Merloni, A., Heinz, S., & di Matteo, T. 2003, MNRAS, 345, 1057
Metzger, B. D., Margalit, B., & Sironi, L. 2019, MNRAS, 485, 4091
Mezcua, M., Suh, H., & Civano, F. 2019, MNRAS, 488, 685
Michilli, D., Seymour, A., Hessels, J. W. T., et al. 2018, Natur, 553, 182
Molina, M., Reines, A. E., Greene, J. E., Darling, J., & Condon, J. J. 2021, ApJ, 910, 5
Mooley, K. P., Margalit, B., Law, C. J., et al. 2022, ApJ, 924, 16
Narayan, R. 1992, RSPTA, 341, 151
Niu, C. H., Aggarwal, K., Li, D., et al. 2022, Natur, 606, 873
Perley, D. A. 2019, PASP, 131, 084503
Peterson, B. M. 1993, PASP, 105, 247
Planck Collaboration, Aghanim, N., Akrami, Y., et al. 2020, A&A, 641, A6
Reines, A. E., Condon, J. J., Darling, J., & Greene, J. E. 2020, ApJ, 888, 36
Reines, A. E., Greene, J. E., & Geha, M. 2013, ApJ, 775, 116
Reines, A. E., & Volonteri, M. 2015, ApJ, 813, 82
Resmi, L., Vink, J., & Ishwara-Chandra, C. H. 2021, A&A, 655, A102
Rickett, B. J., Quirrenbach, A., Wegner, R., Krichbaum, T. P., & Witzel, A. 1995, A&A, 293, 479
Romani, R. W., Narayan, R., & Blandford, R. 1986, MNRAS, 220, 19
Rybicki, G. B., & Lightman, A. P. 1979, Radiative Processes in Astrophysics (New York, NY: John Wiley and Sons, Inc.)
Sabater, J., Best, P. N., Hardcastle, M. J., et al. 2019, A&A, 622, A17
Scholz, P., Spitler, L. G., Hessels, J. W. T., et al. 2016, ApJ, 833, 177

Simard, D., & Ravi, V. 2021, arXiv:2107.11334
Slane, P. 2005, AdSpR, 35, 1092
Smail, I., Hogg, D. W., Yan, L., & Cohen, J. G. 1995, ApJL, 449, L105
Spitler, L. G., Scholz, P., Hessels, J. W. T., et al. 2016, Natur, 531, 202
Staelin, D. H., & Reifenstein, E. C. I 1968, Sci, 162, 1481
Tachibana, Y., & Miller, A. A. 2018, PASP, 130, 128001
Tendulkar, S. P., Bassa, C. G., Cordes, J. M., et al. 2017, ApJL, 834, L7
Ulvestad, J. S. 2009, AJ, 138, 1529
Varenius, E., Conway, J. E., Batejat, F., et al. 2019, A&A, 623, A173
Vedantham, H. K., & Ravi, V. 2019, MNRAS, 485, L78
Voggel, K. T., Seth, A. C., Baumgardt, H., et al. 2019, ApJ, 871, 159
Walker, M. A. 1998, MNRAS, 294, 307
Weisskopf, M. C., Hester, J. J., Tennant, A. F., et al. 2000, ApJL, 536, L81
Wevers, T., Stone, N. C., van Velzen, S., et al. 2019, MNRAS, 487, 4136
Wevers, T., van Velzen, S., Jonker, P. G., et al. 2017, MNRAS, 471, 1694
Xiao, T., Barth, A. J., Greene, J. E., et al. 2011, ApJ, 739, 28